Three-dimensional printing of porous load-bearing bioceramic scaffolds

Page Proof Instructions and Queries

Journal Title: PIH
Article Number: 682984

Greetings, and thank you for publishing with SAGE. We have prepared this page proof for your review. Please respond to each of the below queries by digitally marking this PDF using Adobe Reader (free at https://get.adobe.com/reader).

Please use *only* the circled tools to indicate your requests and responses, as edits via other tools/methods are not compatible with our software. To ask a question or request a formatting change (such as italics), please click the tool and then choose "Text Callout." To access the necessary tools, choose "Comment" from the right-side menu.

Sl. No.	Query
	GQ: Please confirm that all author information, including names, affiliations, sequence, and contact details, is correct.
	GQ: Please review the entire document for typographical errors, mathematical errors, and any other necessary corrections; check headings, tables, and figures.
	GQ: Please ensure that you have obtained and enclosed all necessary permissions for the reproduction of artworks (e.g. illustrations, photographs, charts, maps, other visual material, etc.) not owned by yourself. please refer to your publishing agreement for further information.
	GQ: Please note that this proof represents your final opportunity to review your article prior to publication, so please do send all of your changes now.
	GQ: Please confirm that the acknowledgement, funding and conflict of interest statements are accurate.
1	AQ: Please check whether the expansions inserted for 'HA', 'TCP', 'TTCP' and 'ALP' are correct in Table 1.
2	AQ: Please provide an expansion for 'CAD', if appropriate.
3	AQ: Please provide the location details, such as city, for 'Fritsch GmbH'.
4	AQ: Please provide the location details, such as city, for 'Impact Test Equipment Ltd'.
5	AQ: Please check whether the inserted expansion for 'MD' is correct in Table 3.
6	AQ: Please provide the location details, such as city, for 'Carbolite GmbH'.
7	AQ: Please provide the location details for 'Mitutoyo' and 'MicroPublisher 5.0 RTV'.
8	AQ: Please provide the manufacturer details for 'Kern ABT220-5DM'.
9	AQ: Please provide the location details for 'XRadia/Zeiss VersaXRM-410'.
10	AQ: Please provide the location details for 'Philips XL30 ESEM FEG'.
11	AQ: Please note that some of the references have been renumbered to make their citations sequential in text. Please check.
12	AQ: Please provide location, date and month of conference and publisher details for Ref. 2.
13	AQ: Ref. 27 is not cited in text. Please indicate where a citation should appear or delete the reference.

Special Issue Article

Institution of MECHANICAL ENGINEERS
Journal of ENGINEERING IN MEDICINE

Proc IMechE Part H:
J Engineering in Medicine
1–11

DOI: 10.1177/0954411916682984
pih.sagepub.com
SAGE

Three-dimensional printing of porous load-bearing bioceramic scaffolds

Elena Mancuso[1,2], Naif Alharbi[1], Oana A Bretcanu[1], Martyn Marshall[3], Mark A Birch[4], Andrew W McCaskie[4] and Kenneth W Dalgarno[1]

Abstract

This article reports on the use of the binder jetting three-dimensional printing process combined with sintering to process bioceramic materials to form micro- and macroporous three-dimensional structures. Three different glass-ceramic formulations, apatite–wollastonite and two silicate-based glasses, have been processed using this route to create porous structures which have Young's modulus equivalent to cortical bone and average bending strengths in the range 24–36 MPa. It is demonstrated that a range of macroporous geometries can be created with accuracies of ± 0.25 mm over length scales up to 40 mm. Hot-stage microscopy is a valuable tool in the definition of processing parameters for the sintering step of the process. Overall, it is concluded that binder jetting followed by sintering offers a versatile process for the manufacture of load-bearing bioceramic components for bone replacement applications.

Keywords

Additive manufacturing, three-dimensional printing, bone scaffolds, bioceramics, bioactive glasses

Date received: 14 June 2016; accepted: 15 November 2016

Introduction

Binder jetting first emerged as a rapid prototyping process in the early 1990s.[1] As illustrated in Figure 1, it is a powder bed–based three-dimensional (3D) printing process which selectively jets a liquid binder into the powder in order to consolidate powder layers. The binder may react with the powder to bind it together, or may evaporate to leave a polymer 'glue' which holds the powder together, or both. Through repeated powder re-coating and binder jetting, the process can generate 3D shapes which are a composite or reaction product of the powder and binder, depending on the binding mechanism. The potential to use the process as a method for creating what are known as 'green' bodies, which are parts that need subsequent consolidation through sintering (with the binder sacrificial material and removed as part of the heat treatment), was initially exploited for metal tooling[2] but has since been adopted for a range of sinterable materials. The process can operate either solely with a liquid binder or with the combination of liquid and solid binders. Where a solid binder is used, it is normally part of the powder bed, and normally the intention is that the liquid and solid binders combine in some way to bind the powders together.[3]

The process has been applied to the manufacture of bioceramic parts by a number of research groups. Table 1 summarises previous work with bioceramic scaffolds and the binder jetting approach. While these studies have individually addressed a range of geometries of scaffold and a range of materials, none has assessed in a broad sense the overall capabilities of the process in terms of the requirements for bone replacement applications. The aim of the work presented in this article was to evaluate the capability of the binder jetting/sintering approach to produce load-bearing structures in a range of bioceramic materials and in a range of microporous and macroporous shapes, in order to assess the suitability of the process as a method of creating load-bearing implants for bone replacement applications.

[1]School of Mechanical and Systems Engineering, Newcastle University, Newcastle upon Tyne, UK
[2]School of Mechanical Engineering, University of Leeds, Leeds, UK
[3]Glass Technology Services Ltd, Sheffield, UK
[4]Division of Trauma and Orthopaedic Surgery, University of Cambridge, Cambridge, UK

Corresponding author:
Elena Mancuso, School of Mechanical Engineering, University of Leeds, Woodhouse Lane, Leeds LS2 9JT, UK.
Email: e.mancuso@leeds.ac.uk

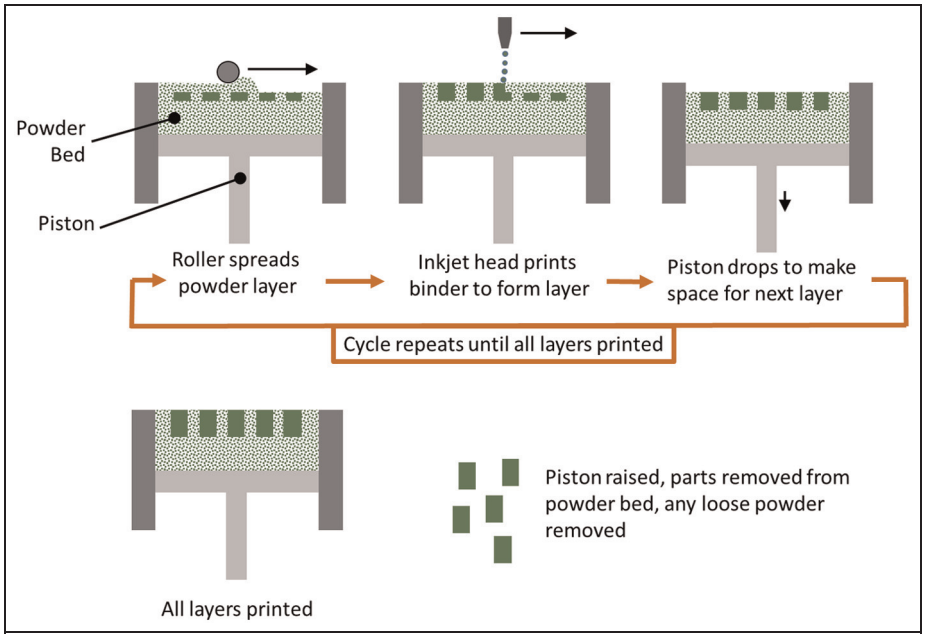

Figure 1. Binder jetting 3D printing process.

Table 1. Summary of previous studies of binder jetting/sintering of bioceramics. .

AQ1

Material	Sintering condition	Mechanical properties	Biological properties	References
HA	1250 °C/2 h	Compressive strength: 21.2 ± 2.2 MPa (dense part)	Cells were seeded on the scaffolds and cultivated under static and dynamic setups. This last method showed better results with a deep cell proliferation into the HA structure	Leukers et al.[4] and Seitz et al.[5]
HA	1250 °C/2 h	Compressive strength: 21.2 ± 2.2 MPa (dense part)	Cell viability tests showed superior biocompatibility of HA scaffolds to Bio-Oss®	Seitz et al.[5] and Warnke et al.[6]
β-TCP	1400 °C	Compressive strength: 8.66 ± 0.11 MPa (% porosity 46.07 ± 8.52)	In vitro cytotoxic assays showed a good cell–scaffold interaction, thus revealing the scaffolds' biocompatibility	Santos et al.[7]
β-TCP/Bioglass	1000 °C	Bending strength: 14.9 ± 3.6 MPa	–	Bergmann et al.[8]
HA/AW	1300 °C/3 h	Bending strength: 35.22 ± 6.56 MPa (% porosity 30.00 ± 1.50)	In vitro tests showed that osteoblast cells attach and attain normal morphology on the surface of the 3D-printed scaffolds	Suwanprateeb et al.[9]
Brushite	–	Bending strength: 5.2 MPa	In vivo implantation of both brushite and monetite scaffolds showed their osteoinductive potential.	Habibovic et al.[10] and Klammert et al.[11]
Monetite	134 °C/2 h	Bending strength: 3.9 MPa		
TTCP/β-TCP	1200 °C/6 h 1400 °C/6 h	Compressive strength: 1.3 ± 0.1 MPa 3.9 ± 0.1 MPa	MC3T3-E1-cells grew on the scaffolds as adherent cells showing the increase in ALP activity over the 3 weeks in culture	Khalyfa et al.[12]
TTCP/$CaSO_4$	1000 °C/6 h	Compressive strength: 0.1 ± 0.01 MPa	–	

HA: hydroxyapatite; TCP: tri-calcium phosphate; TTCP: tetra calcium phosphate; AW: apatite–wollastonite; ALP: alkaline phosphatase.

AQ2

Table 2. Part designs.

Name	Shape	CAD dimensions	Purpose	Material
Bars with channels	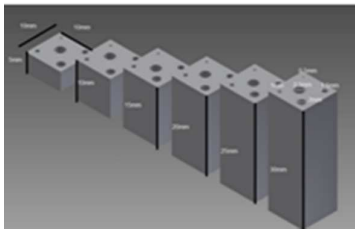	10 × 10-square cross section Height: 5–30 mm in 5-mm increments 1–2 mm diameter through channels	Assessment of minimum achievable channel diameter	AW1
Beam	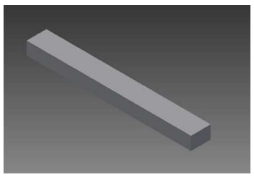	50 × 5 × 4 mm	Three-point bending test	NCL2, NCL7, AW4
Disc	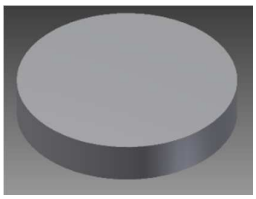	Diameter: 10.25 mm; height: 2.25 mm	Porosity and morphology	NCL2, NCL7, AW4, AW5
Disc with pockets	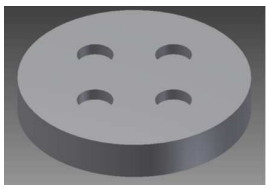	As above, with pockets 1.5 mm diameter and 0.5 mm depth	Accuracy of small features	AW1
Hollow cylinder	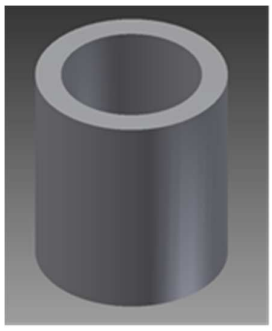	Height: 8.42 mm, outer diameter: 7.48 mm, wall thickness: 2 mm	Accuracy of thin-walled structure	AW5

AW: apatite–wollastonite.

Materials and methods

Part designs

A series of parts were designed to evaluate the ability of the process to produce specific features with dimensions in the range 0.5–40 mm. These are presented in Table 2, which also outlines the rationale for the choice of the individual designs.

Powder blend preparation

Three different base glasses were processed in this study: apatite–wollastonite (AW) and two novel glasses developed by Newcastle University (Newcastle upon Tyne, UK) in collaboration with Glass Technology Services (GTS) Ltd (Sheffield, UK) designated as NCL2 and NCL7.[13] The composition of the materials is outlined in Table 3. The glasses were produced and supplied by GTS Ltd. All the glasses were prepared through a melt-quenching route, in which the components of each formulation were weighed, mixed, melted, and quenched in water to produce frits. The glass frits were crushed into a one-bowl zirconia ball milling machine (Planetary Mono Mill Pulverisette 6; Fritsch GmbH, Germany) using a rotational speed of 400 r/min for 30 min (10 min each repetition). The obtained powders were then sieved using a mechanical sieve shaker (Impact Test Equipment Ltd, UK) to obtain specific particle size. The glass powders were then blended with maltodextrin powder (0–53 μm; Oneon, Bristol, UK), as a solid binder, in the ratios listed in Table 3, for 1 h using a roller mixer (Stuart Roller Mixer SRT6;

AQ3

AQ4

Table 3. Composition of the glasses (wt%) and powder blends (wt%). AQ5

Code	Glass composition (wt%)	Powder blend composition
NCL2	$36.90SiO_2$–$9.70P_2O_5$–$1.90B_2O_3$–$3.39Na_2O$–$11.48CaO$–$3.85K_2O$–$4.41MgO$–$2.38MnO_2$–$6.97Al_2O_3$–$2.13CaF_2$–$10.92Fe_2O_3$–$0.41Li_2O$–$1.97MoO_3$–$1.52SeO_2$–$2.07Cr_2O_3$	70 wt% NCL2: 0–53 μm 30 wt% MD: 0–53 μm
NCL7	$39.96SiO_2$–$9.46P_2O_5$–$12.39Na_2O$–$11.19CaO$–$2.50K_2O$–$1.61MgO$–$15.44AgO$–$2.13TiO_2$–$4.26Fe_2O_3$–$1.06CuO$	70 wt% NCL2: 0–53 μm 30 wt% MD: 0–53 μm
AW1	4.6 MgO–44.7 CaO–34 SiO_2–16.2 P_2O_5–0.5 CaF_2	70 wt% AW: 54–90 μm 30 wt% MD: 0–53 μm
AW4	4.6 MgO–44.7 CaO–34 SiO_2–16.2 P_2O_5–0.5 CaF_2	70 wt% AW: 0–53 μm 30 wt% MD: 0–53 μm
AW5	4.6 MgO–44.7 CaO–34 SiO_2–16.2 P_2O_5–0.5 CaF_2	55 wt% AW: 54–90 μm 15 wt% AW: 0–53 μm 30 wt% MD: 0–53 μm

AW: apatite–wollastonite; MD: maltodextrin.

Camlab, Over, UK). Previous work[14] indicated that using 30% maltodextrin as a solid binder gave green parts which were sufficiently well consolidated to be handled and which could be effectively sintered.

2.3 X-ray powder diffraction analysis

X-ray powder diffraction (XRD) analysis was performed using a PANalytical X'Pert Pro MPD, powered by a Philips PW3040/60 X-ray generator fitted with an X'Celerator detector. Diffraction data were acquired by exposing powder samples to Cu-K_α X-ray radiation, which was supplied with 40 kV, and a current of 40 mA.

The data were collected over a 2θ range between 5° and 80° 2θ, with a step size equal to 0.0334°, a counting time per step of 200 s using the scanning X'Celerator detector. Fixed anti-scatter and divergence slits of 1° were used together with a beam mask of 10 mm. All scans were carried out in 'continuous' mode.

Phase identification was carried out by means of the PANalytical X'Pert HighScore Plus© software, in conjunction with the International Centre for Diffraction Data (ICDD) Powder Diffraction File 2 Database (2004), ICDD Powder Diffraction File 4 – Minerals (2014) and the Crystallography Open Database (February 2013; www.crystallography.net).

Powder thermal characterisation

The sintering behaviour of the NCL2 and NCL7 glass powders was characterised using a hot-stage microscope (Misura®; Expert System Solutions, Modena, Italy). Specimens were prepared by manually pressing glass powders into a small cylindrical die (2 mm in diameter and 3 mm in height) to make a cylindrical powder compact, which then was placed onto a 10 × 15 × 1-mm alumina plate, before being heated to a maximum of 1450 °C, and at a rate of 10 °C/min.

Indirect 3D printing of green parts

A commercial ZPrinter® 310 Plus 3D printer (Z Corporation, Rock Hill, SC USA) was used to print all parts. A layer thickness of 0.1 mm was used, with the liquid binder zb®60 clear binder (Z Corporation). When jetting the binder, the outer shell of a layer is normally more saturated with binder in order to give the outside of the part more definition, and the machine control parameter which defines this is the binder/volume ratio. In this case, the binder/volume ratio of the shell was 0.21 and that of the inner core of the layers was 0.1. Green parts were printed with the parts oriented in the powder bed, as shown in Table 2, and were left to dry overnight before being removed from the build area, and then cleaned of any loose powder using an air blower. Green parts were then sintered in a furnace (Carbolite 1200 CWF; Carbolite GmbH, Germany) at temperatures of up to 1250 °C, with the sintering cycle for the NCL2 and NCL7 materials based on the hot-stage microscopy results and the sintering cycle for the AW material based on a previous work with this material.[15] AQ6

Scaffold dimensions, porosity and microarchitecture

Dimensional measurements were made using a digital caliper (Mitutoyo, UK, with a resolution of 0.02 mm) and a digital microscope (Olympus MicroPublisher 5.0 RTV). Levels of open porosity were measured according to the BS EN 623-2:1993 using Archimedes' method. Samples were weighed by means of a density determination kit in an analytical balance (Kern ABT220-5DM). The dry weight of the samples was recorded as m_1. Then, they were immersed in distilled water until no bubbles emerged from the water beaker and the submerged mass (m_3) was measured. Afterward, the specimens were taken out and re-weighed to calculate the wet mass (m_2) in air. The porosity was then calculated as follows AQ7 AQ8

$$Open\ porosity(\%) = \frac{(m_2 - m_1)}{(m_2 - m_3)} \times 100 \quad (1)$$

Five specimens for each group were tested to calculate the average porosity. The results were expressed as mean ± standard deviation (SD).

The total porosity, given by the sum of the close and open porosity, was calculated according to the following equation

$$Total\ porosity(\%) = \left(1 - \frac{m_1}{\rho V_s}\right) \times 100 \quad (2)$$

where ρ is the density of the material, and V_s is the outer volume of the porous sample. Five specimens for each group were tested to calculate the average porosity. The results were expressed as mean ± SD.

Scaffold architecture and structural interconnectivity were also investigated by micro-computed tomography (micro-CT; XRadia/Zeiss VersaXRM-410). The scanner was set at a voltage between 60 and 80 kV and a current of 248 A, and the samples were scanned with an isotropic voxel size of 2.4 μm with approximately 1600 slices covering the sample height. Afterward, the scanned two-dimensional (2D) slices were reconstructed to give 3D views of the entire structure using Avizo Fire software.

Mechanical property testing

The mechanical properties of the 3D-printed structures were assessed by three-point bending test using an Instron 5567 testing machine (Instron Corp., Canton, MA, USA). The tests were performed according to ASTM C1161 – 13 Standard. Specimens were 3D printed as beams (Table 2), during the tests, the crosshead speed of the machine was set at 1 mm/min, and the support span length was 30 mm. A load cell of 1 kN was used, and the results, obtained from testing five samples, were expressed as the average values ± SD.

The flexural strength (σ_f) was calculated according to the following equation

$$\sigma_f = \frac{3PL}{2bd^2}$$

where P represents the applied load (N), L (mm) is the support span length, b (mm) is the sample width and d is the depth (mm). The flexural modulus (E_f) was calculated according to the following equation

$$E_f = \frac{L^3 m}{4bd^3}$$

where L (mm) represents the support span length, m (N/mm) is the gradient (i.e. slope) of the initial linear part of the load–deflection, b (mm) is the sample width and d (mm) is the sample depth.

Microscopy

Microstructural observations were performed by scanning electron microscope (Philips XL30 ESEM FEG) on glass powders, green bodies and sintered structures. Before image acquisition, the samples were attached to an aluminium stub, then sputtered with a thin layer of gold in an argon-purged chamber (approximately 10 nm, sputter time 40 s at 40 mA) and afterward analysed. All the images were taken at an operation voltage of 20 kV, with a working distance of between 5 and 10 mm.

Results

Precursors

Microstructural analysis. SEM micrographs of the raw glass powders are shown in Figure 2. All the compositions were characterised by sharp edge and irregular shape particles. Furthermore, it can be observed that for all the glasses, most of the particles were very fine (ranging from 20 to 53 μm), with the presence also of grains smaller than 10 μm, which tended to compact producing aggregates.

Thermal behaviour. Figure 3 shows the hot-stage microscopy results. NCL2 and NCL7 specimens maintained their initial rectangular shape before the first shrinkage temperature (T_{FS}), which was at around 600 °C. At temperatures higher than the T_{FS}, the samples started to shrink until the temperature of maximum shrinkage (T_{MS}), after which the samples expanded until they reached their temperature of maximum volume (T_{MV}). The AW specimen broadly maintained its shape until melting.

A three-step heating treatment, as shown in Figure 4, was developed for NCL2 and NCL7.[13] The first step (5 °C/min) was to remove completely the sacrificial binders without losing sample integrity, the second was to promote nucleation of the glass particles and the third

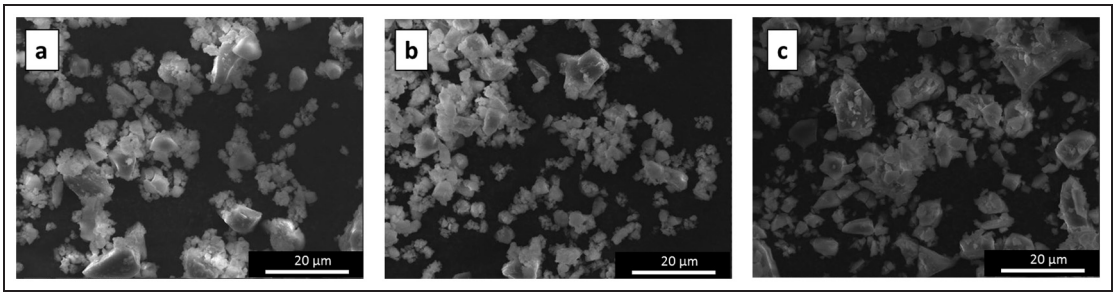

Figure 2. SEM analysis (magnification 1500×) showing the glass powders morphology: (a) NLC2, (b) NCL7 and (c) AW.

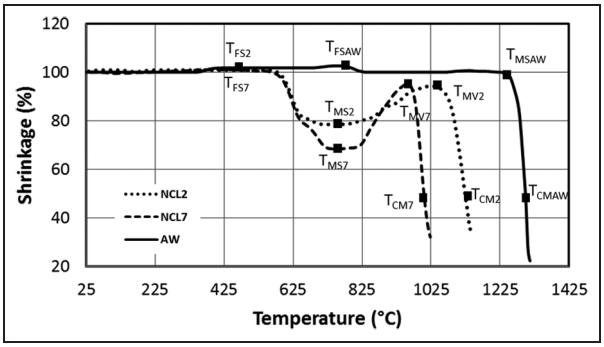

Figure 3. Shrinkage profile derived from hot-stage microscopy as function of temperature for NCL2, NCL7 and AW compositions (T_{FS} = temperature of first shrinkage, T_{MS} = temperature of maximum shrinkage, T_{MV} = temperature of maximum volume, T_{CM} = temperature of complete melting).

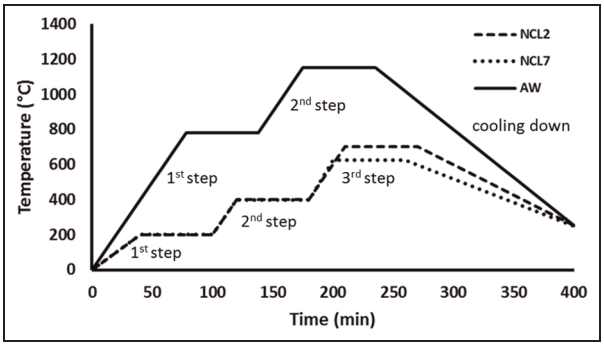

Figure 4. Heat treatment profiles for NCL2, NCL7 and AW green bodies.

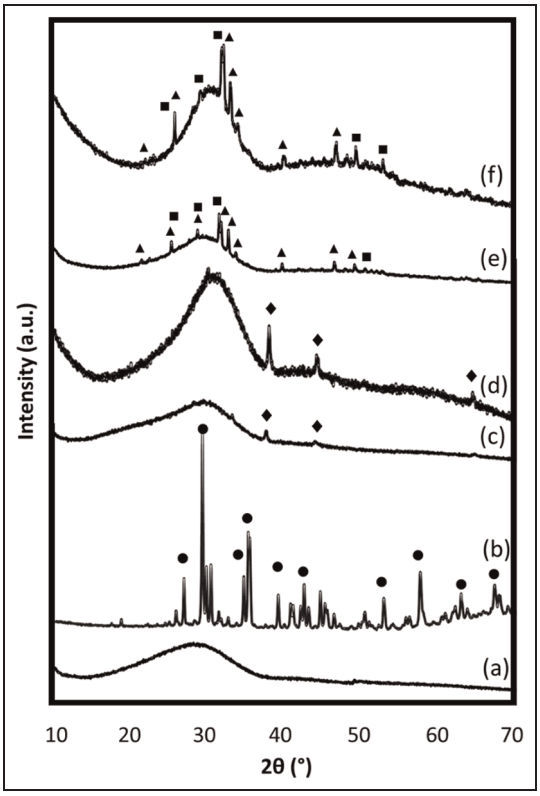

Figure 5. XRD patterns of (a) glass powder and (b) pellet sintered at 700 °C of NCL2 composition (● – diopside), (c) glass powder and (d) pellet sintered at 625 °C of NCL7 composition (♦– silver) and (e) glass powder and (f) pellet sintered at 850 °C of AW composition (▲ – hydroxyapatite, ■ –β-wollastonite).

was the sintering step (at 700 °C and 625 °C for NCL2 and NCL7, respectively) to consolidate the final structure. Figure 4 also illustrates the heat treatment used for AW.

XRD analysis. XRD patterns for all three compositions before and after sintering are reported in Figure 5. Figure 5(a) and (b) shows that crystalline phases developed during the sintering treatments of the NCL2 formulation, which changed its status from a completely amorphous material to a glass-ceramic. These were identified as diopside phase ($CaMg(SiO_3)_2$; ICDD ref. code 01-073-6374). The NCL7 formulation was almost amorphous (Figure 5(c)), as a very low amount of Ag was detected before the sintering treatment. The intensity of Ag peaks (ICDD ref. code 04-003-1425) increased after sintering (Figure 5(d)). Figure 5(e) and (f) shows that for AW, the crystalline phases remained the same (hydroxyapatite and β-wollastonite) after the sintering process, but that the sintered material showed more intense peaks (Figure 5(f)) with respect to the raw glass powder (Figure 5(f)), confirming the glass-ceramic nature of this formulation.

Sintered scaffolds

Microstructure and shrinkage. Figure 6 shows representative images of the 3D-printed bioceramic samples after sintering, with Figure 7 showing representative surface morphologies. The sintered structures exhibited a very high degree of densification, with volume reductions between 34.55% ± 3.67% and 57.24% ± 2.8 3%, and with shrinkage varying with material, powder blend and shape as reported in Table 4. The resulting

Table 4. Average volumetric shrinkage (%) for selected sintered samples (n = 10) (mean ± SD).

	NCL2	NCL7	AW1	AW4	AW5
Beam	42.41 ± 3.43	47.04 ± 2.54	34.55 ± 3.67	48.56 ± 2.12	41.30 ± 5.34
Disc	49.66 ± 1.55	57.24 ± 2.83	–	49.07 ± 2.55	–

AW: apatite–wollastonite; SD: standard deviation.

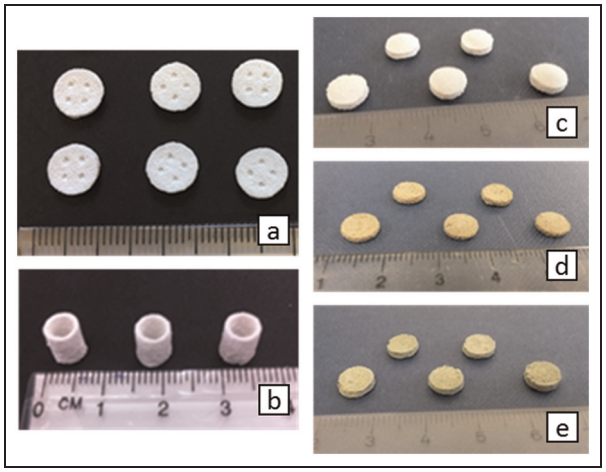

Figure 6. Representative images of the 3D-printed bioceramic structures after sintering: (a) disc with pocket AW1, (b) hollow cylinder AW5, (c) disc AW4, (d) disc NCL2 and (e) disc NCL7.

morphologies were very similar for all powder blends, with a rough surface and an interconnected 3D network. The original sharp grain boundaries of the glass powders were no longer distinguishable, indicating that the thermal treatment led to neck formation and consolidation (see red arrows in Figure 7).

Process capabilities. Table 5 summarises the porosities and accuracies achieved in the manufacture of a range of geometries. The most variable dimension in absolute terms was the length of the beams, which gave a mininum–maximum range of 0.46 mm, with the smaller dimensions showing less variation. The variations in open porosity are significant, varying from 12% to 33%. However, it is notable that the variations for the individual batches of parts are quite small: the variations between the different part designs were much larger than those from part to part within a specific build. In generating macroporous structures using the process, the main limitation is the removal of unwanted powder from channels. Figure 8 illustrates that the minimum achievable cylindrical channel diameter was 1–2 mm, depending on the length of the channel. Figure 9 illustrates both open and total porosity measures for all five powder blends and indicates that the total porosity varied from 28% to 50%, but typically only half of the total porosity is accessible.

Micro-CT analysis. 3D reconstructions of the sintered bioceramic structures based on micro-CT analysis are shown in Figure 10. NCL2 showed a low level of microporosity, showing a heterogeneous distribution of pores. Additionally, in Figure 10(a), the presence of macro-channels of around 150–400 μm in size, which crossed the structure, can be observed. NCL7, AW4 and AW5 all showed an architecture characterised by a network of connected micropores, typically less than

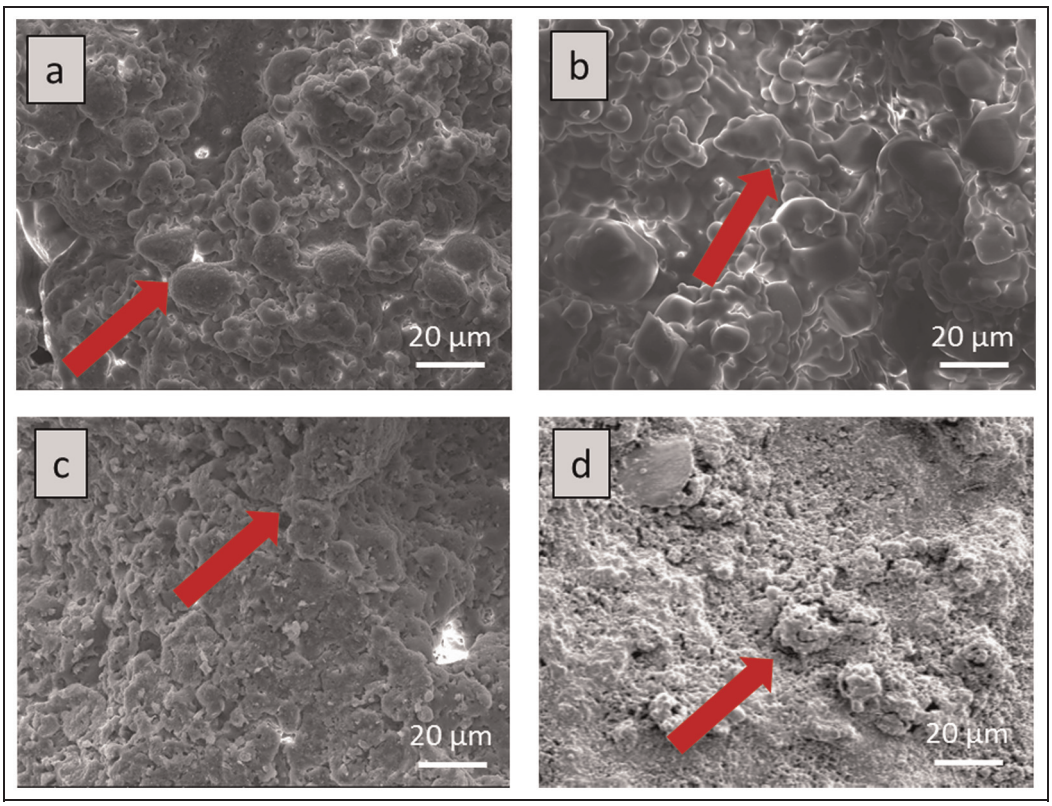

Figure 7. SEM micrographs of surfaces of (a) NCL2, (b) NCL7, (c) AW4 and (d) AW5 3D-printed structures after sintering (red arrows indicate necking formation).

Table 5. Summary of process capabilities.

Part name and material	Open porosity mean ± SD (%)	Least consistent dimension	For least consistent dimension		
			Mean ± SD (mm)	Max. (mm)	Min. (mm)
Beam AW5	12.40 ± 0.29	Length	40.67 ± 0.06	40.96	40.50
Disc AW1	14.20 ± 0.19	Diameter	7.94 ± 0.03	8.11	7.85
Disc with pockets AW1	28.78 ± 1.08	Pocket depth	0.48 ± 0.01	0.60	0.40
Disc AW4	22.48 ± 1.55	Diameter	8.09 ± 0.05	8.30	7.90
Disc NCL2	15.78 ± 1.12	Diameter	7.42 ± 0.02	7.56	7.28
Disc NCL7	23.41 ± 0.94	Diameter	7.54 ± 0.12	7.92	7.12
Hollow cylinder AW5	33.29 ± 1.17	Wall thickness	1.03 ± 0.03	1.16	0.95

AW: apatite–wollastonite; SD: standard deviation.

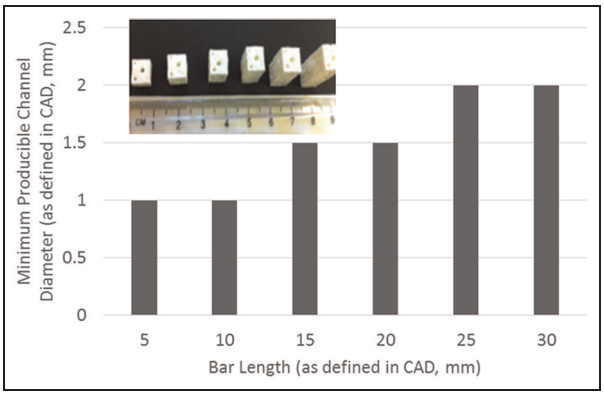

Figure 8. Minimum producible channel diameter as a function of channel length. Inset image shows sintered bars.

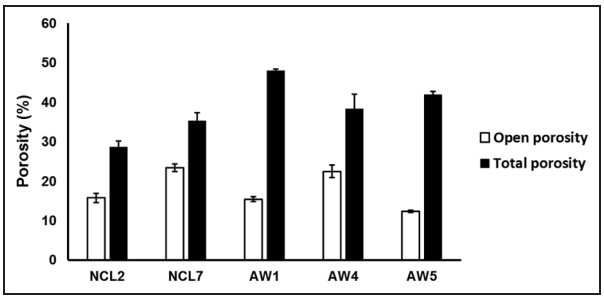

Figure 9. Averaged open and total porosity values for sintered NCL2, NCL7 and AW4 3D-printed discs and AW1 and AW5 3D-printed beams. In each case measured for a batch of 10 parts. Error bars represent the standard deviation.

150 μm in size, with AW5 showing the most homogeneous and widespread network of pores. The AW1 blend produced a part with large pores (approximately 0.5–1 mm) distributed through the structure.

Mechanical properties. A summary of the values of mechanical properties for NCL2, NCL7 and AW1-printed beams is reported in Table 6. NCL2 was characterised by the highest mechanical properties. However, no significant differences were found for the novel 3D-printed scaffolds in comparison with AW, whereas NCL2 scaffolds showed flexural strength values significantly higher than NCL7 beams.

Typical load–deflection curves for NCL2, NCL7 and AW4 are presented in Figure 11. The traces show evidence of the beams slipping in the supports, and of localised failure, which was concentrated at the loading points.

Discussion

Sintering cycle development

Utela et al.[16,17] presented a comprehensive overview of the steps involved in optimising the binder jetting and sintering processes. The most significant enhancement we would propose is the use of a heating microscope to understand the thermal behaviour of the materials and identify sintering temperatures. This technique allowed the quantification of the sintering interval of a compound by measuring the variation of the sample dimensions during the heating treatment,[18] and the good mechanical properties shown in Table 6 indicates that the chosen sintering temperatures were effective.

Process capabilities

Taken altogether, the results presented in this article indicate that binder jetting followed by sintering with glass powders can produce bioceramic parts:

- For which the evolution of different material phases during sintering can be controlled through selection

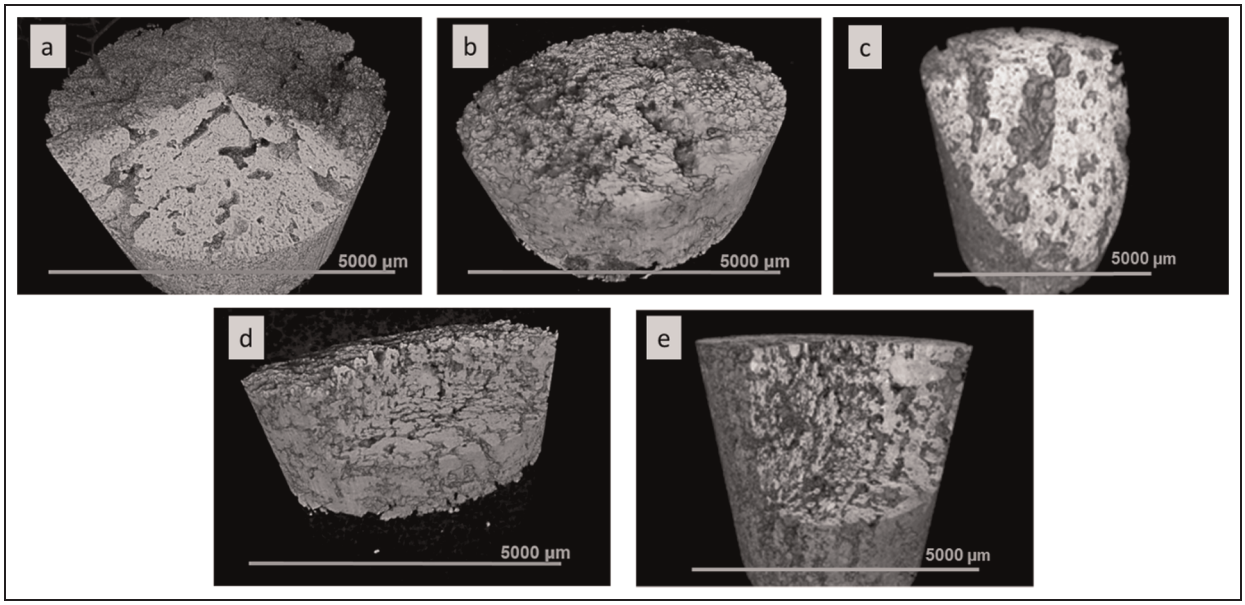

Figure 10. 3D reconstruction of (a) NCL2, (b) NCL7, (c) AW1, (d) AW4 and (e) AW5 obtained through micro-CT analysis.

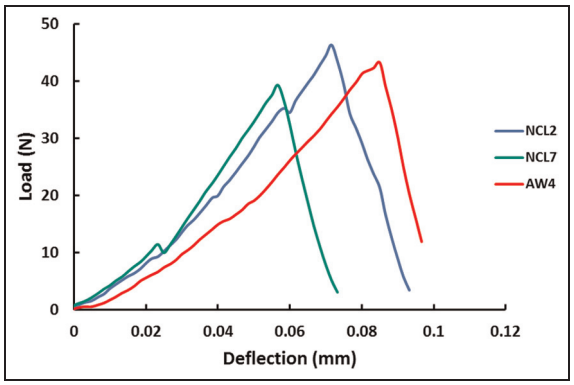

Figure 11. Representative load–deflection traces for 3D-printed NCL2, NCL7 and AW4 porous ceramic beams, resulting from the three-point bending test.

Table 6. Summary of the mechanical properties (mean ± SD) for 3D-printed NCL2, NCL7 and AW porous scaffolds assessed by three-point bending test.

Sample	Flexural strength (MPa)	Flexural modulus (GPa)
NCL2	35.84 ± 2.52	13.47 ± 1.73
NCL7	26.08 ± 2.14	11.20 ± 0.92
AW1	23.65 ± 0.73	7.27 ± 0.52
AW4	28.64 ± 3.26	10.86 ± 1.18
AW5	25.95 ± 1.59	11.18 ± 0.94

AW: apatite–wollastonite; SD: standard deviation; 3D: three-dimensional.

of an appropriate sintering regime, as illustrated by the XRD spectra in Figure 5.

- With mechanical properties in a porous part which mean that they can be applied in load-bearing applications, and with a modulus which matches the modulus range shown by cortical bone,[19–21] as indicated by Table 6.
- With a significant degree of microporosity, and the scope to design macroscopic channels with diameters of over 1 mm, as indicated by Figures 6 and 8. This combination of micro- and macroscopic channels is desirable as the microporosity allows bone ingrowth for implant integration, while macroporous volumes within a scaffold allow for bone regeneration, and the effectiveness of this microporous/macroporous structure has previously been shown in vitro with the AW material.[22]
- Which are accurate to ±0.25 mm over length scales from 0.5 to 40 mm, as indicated in Table 5.

This combination of capabilities, together with appropriate choice of materials, makes binder jetting combined with sintering an attractive process for the creation of load-bearing bone replacement devices. The success of such devices depends not only on the mechanical properties at the point of implantation but also on (1) the bioactivity of the materials and (2) the evolution of the mechanical properties in vivo. AW as a material is known to be bioactive,[22,23] and it has previously been used to produce commercial medical devices. AW is known to be a slowly resorbing material when porous[24] and would resorb at a rate which was slower than the rate at which bone can regenerate, and degradation studies on NCL2 and NCL7 indicate that they also resorb slowly.[13] This combination of properties would give a device which was load bearing at the point of implantation, supported bone ingrowth into the microporous structure for integration within the body and which then slowly resorbed to be replaced by natural bone. Ceramic materials on their own are brittle, which is why the ingrowth and gradual resorption

to be replaced by natural bone are important elements in the device design.

Overall, porosity levels can also clearly be influenced by device design. Table 4 makes it clear that shrinkage during sintering varied non-significantly with both material and shape, and no clear trend was observed in this. The increased open porosity of the hollow cylinder in Table 5 when compared to the beams or discs is considered to be in part due to the increased surface area/volume ratio of that shape, and if the hollow channel is considered to be a pore, then the overall porosity of the structure, compared to a solid cylinder of the same external dimensions would be ~63%.

While the porous nature of the sintered materials and the scope for macroporous device design mean that large porosities are possible, Table 5 indicates that there is still some room for improvement in terms of the quality and repeatability of the porosity. It would be preferable for more of the closed porosity to be open and for the porosity levels to be more consistent. Most of the variations shown in Table 5 are considered to have arisen from build to build variations in powder blends. Mixing particle size ranges is inherently more stochastic than mixing particles with closely defined particle sizes, and there is scope for variations in powder blend composition within the blending protocol outlined in section 'Powder blend preparation'. In addition, powder sieving is not a completely reliable process: high-aspect-ratio powder particles can pass through sieves to give large particles in a small size fraction, and agglomerated small particles may not pass through a sieve to reach their natural size fraction. Variations arising from powder processing could then produce differences in both the powder bed (and therefore in the green part) and the sintering behaviour which would produce differences in the quality of the porosity. Better control of the starting powder blend particle sizes and quality are considered to offer the most likely route to both consistency overall and to making the closed porosity more open (for instance, through producing a blend with a greater proportion of larger, more spherical, particles).

The main limitation identified in this study is the levels of shrinkage. For the relatively small parts created in this study, volume shrinkage levels of around 50% did not cause any gross distortions in geometry, and the shrinkage was in general isotropic. However, with larger parts or more complex geometries, even isotropic shrinkage can be a problem,[25] and so, there are likely to be size and shape limitations on parts. The development of alternative binder systems which reduce the volume of binder material used would be the process improvement that would reduce the shrinkage and therefore the scale of the limitation.[26]

Conclusion

Binder jetting followed by sintering offers a versatile process for the manufacture of load-bearing bioceramic components for bone replacement applications. The results presented in this article show that the process can produce parts in a range of sinterable bioceramics which are accurate to within ± 0.25 mm and have micro and macroporous structures, with mechanical properties which approach or match those of cortical bone.

Acknowledgements

Naif Alharbi would like to acknowledge the support from the Saudi Arabian government for his PhD studentship. The help of the Politecnico do Torino in performing the hot-stage microscope studies is gratefully acknowledged. The micro-CT studies were performed at the Durham XRCT Facility with the support of its staff and this is also gratefully acknowledged.

Declaration of conflicting interests

The author(s) declared no potential conflicts of interest with respect to the research, authorship and/or publication of this article.

Funding

This work reported in this paper was partly funded by the Arthritis Research UK Tissue Engineering Centre (19429), the EC Framework VII Restoration (280575) project and the EPSRC Centre for Innovative Manufacturing in Medical Devices (EP/K029592).

References

1. Sachs E, Cima M, Williams P, et al. Three dimensional printing: rapid tooling and prototypes directly from a CAD model. *J Eng Ind: T ASME* 1992; 114(4): 481–488. AQ11
2. Sachs E, Allen S, Guo H, et al. Progress on tooling by 3D printing; conformal cooling, dimensional control, surface finish and hardness. In: *Proceedings of solid free-form fabrication symposium*, 1997. AQ12
3. Bose S, Vahabzadeh S and Bandyopadhyay A. Bone tissue engineering using 3D printing. *Mater Today* 2013; 16(12): 496–504.
4. Leukers B, Gülkan H, Irsen SH, et al. Hydroxyapatite scaffolds for bone tissue engineering made by 3D printing. *J Mater Sci: Mater Med* 2005; 16(12): 1121–1124.
5. Seitz H, Rieder W, Irsen S, et al. Three-dimensional printing of porous ceramic scaffolds for bone tissue engineering. *J Biomed Mater Res B* 2005; 74(2): 782–788.
6. Warnke PH, Seitz H, Warnke F, et al. Ceramic scaffolds produced by computer-assisted 3D printing and sintering: characterization and biocompatibility investigations. *J Biomed Mater Res B* 2010; 93(1): 212–217.
7. Santos CFL, Silva AP, Lopes L, et al. Design and production of sintered β-tricalcium phosphate 3D scaffolds for bone tissue regeneration. *Mater Sci Eng C* 2012; 32(5): 1293–1298.
8. Bergmann C, Lindner M, Zhang W, et al. 3D printing of bone substitute implants using calcium phosphate and bioactive glasses. *J Eur Ceram Soc* 2010; 30(12): 2563–2567.
9. Suwanprateeb J, Sanngam R, Suvannapruk W, et al. Mechanical and in vitro performance of apatite-wollastonite

glass ceramic reinforced hydroxyapatite composite fabricated by 3D-printing. *J Mater Sci: Mater Med* 2009; 20(6): 1281–1289.
10. Habibovic P, Gbureck U, Doillon CJ, et al. Osteoconduction and osteoinduction of low-temperature 3D printed bioceramic implants. *Biomaterials* 2008; 29(7): 944–953.
11. Klammert U, Gbureck U, Vorndran E, et al. 3D powder printed calcium phosphate implants for reconstruction of cranial and maxillofacial defects. *J Cranio Maxill Surg* 2010; 38(8): 565–570.
12. Khalyfa A, Vogt S, Weisser J, et al. Development of a new calcium phosphate powder-binder system for the 3D printing of patient specific implants. *J Mater Sci: Mater Med* 2007; 18(5): 909–916.
13. Mancuso E. *Processing and characterisation of novel bioceramics for load bearing applications*. Newcastle upon Tyne: Newcastle University, 2016.
14. Alharbi NA. *Indirect three dimensional printing of apatite-wollastonite structures for biomedical applications*. Newcastle upon Tyne: Newcastle University, 2015.
15. Xiao K, Dalgarno KW, Wood DJ, et al. Indirect selective laser sintering of apatite-wollostonite glass-ceramic. *Proc IMechE, Part H: J Engineering in Medicine* 2008; 222(7): 1107–1114.
16. Utela B, Storti D, Anderson R, et al. A review of process development steps for new material systems in three dimensional printing (3DP). *J Manuf Process* 2008; 10(2): 96–104.
17. Utela BR, Storti D, Anderson RL, et al. Development process for custom three-dimensional printing (3DP) material systems. *J Manuf Sci E: T ASME* 2010; 132(1): 0110081–0110089.
18. Bretcanu O, Chatzistavrou X, Paraskevopoulos K, et al. Sintering and crystallisation of 45S5 Bioglass® powder. *J Eur Ceram Soc* 2009; 29(16): 3299–3306.
19. Goldstein SA. The mechanical properties of trabecular bone: dependence on anatomic location and function. *J Biomech* 1987; 20(11–12): 1055–1061.
20. Keaveny TM and Hayes WC. Mechanical properties of cortical and trabecular bone. In: Hall BK (ed.) *Bone a treatise, volume 7: bone growth*. Boca Raton, FL: CRC Press, 1993, pp.285–344.
21. Rho J-Y, Kuhn-Spearing L and Zioupos P. Mechanical properties and the hierarchical structure of bone. *Med Eng Phys* 1998; 20(2): 92–102.
22. Lee JA, Knight CA, Kun X, et al. In vivo biocompatibility of custom-fabricated apatite-wollastonite-mesenchymal stromal cell constructs. *J Biomed Mater Res A* 2015; 103(10): 3188–3200.
23. Dyson JA, Genever PG, Dalgarno KW, et al. Development of custom-built bone scaffolds using mesenchymal stem cells and apatite-wollastonite glass-ceramics. *Tissue Eng* 2007; 13(12): 2891–2901.
24. Ohsawa K, Neo M, Okamoto T, et al. In vivo absorption of porous apatite- and wollastonite-containing glass-ceramic. *J Mater Sci: Mater Med* 2004; 15(8): 859–864.
25. Butscher A, Bohner M, Roth C, et al. Printability of calcium phosphate powders for three-dimensional printing of tissue engineering scaffolds. *Acta Biomater* 2012; 8(1): 373–385.
26. Cox SC, Thornby JA, Gibbons GJ, et al. 3D printing of porous hydroxyapatite scaffolds intended for use in bone tissue engineering applications. *Mater Sci Eng C Mater Biol Appl* 2015; 47: 237–247.
27. Tadic D and Epple M. A thorough physicochemical characterisation of 14 calcium phosphate-based bone substitution materials in comparison to natural bone. *Biomaterials* 2004; 25(6): 987–994.

AQ13